



Cite this: *Sustainable Energy Fuels*,  
2019, 3, 422

## Computation and assessment of solar electrolyzer field performance: comparing coupling strategies

Gowri M. Sriramagiri, <sup>\*ab</sup> Wesley Luc, <sup>c</sup> Feng Jiao, <sup>c</sup> Kathy Ayers, <sup>d</sup>  
Kevin D. Dobson <sup>a</sup> and Steven S. Hegedus <sup>ab</sup>

Carbon-free solar fuel generation through use of photovoltaic-driven electrolyzers (PV-ECs) and photoelectrochemical cells (PECs) has recently grown to be a subject of much interest. Advancements have been provided through improved catalytic activity, high-performance tandem PV and extensive materials exploration, development and characterization. The generally accepted figure of merit is solar-to-fuel efficiency (SFE), measured with the device at standard testing conditions (STC) at '1 sun' *i.e.*, 1000 W m<sup>-2</sup> insolation, clear sky spectrum, and 25 °C operating temperature. However, this does not offer a comprehensive measure of system performance as actual field operating conditions are rarely close to those used for testing. A thorough understanding of PV-EC field performance under realistic operating conditions can assist in holistic device design and scalability. Here, a model is developed to compute their real-life performance using hourly variation in solar irradiance and air temperature over a one-year period. It is then applied to two systems: a previously reported bench-scale high-efficiency CO<sub>2</sub> PV-EC and a MW-scale solar H<sub>2</sub>O electrolysis system conceptually designed employing commercial solar panels and water electrolyzers. While the use of DC power optimizer devices was shown to increase annual gas yield by up to 5% for an optimally-matched directly-coupled system, the benefit is shown to be much higher for even slightly mismatched systems.

Received 1st August 2018  
Accepted 23rd October 2018

DOI: 10.1039/c8se00399h

rsc.li/sustainable-energy

### 1. Introduction

While the ability to source renewable electricity has achieved considerable technological maturity and dramatically lower costs in the past decade, it is now imperative to focus attention towards reliable energy storage, transportation and/or dispatchable generation of fuels to realize the sustainable energy infrastructure of the future. A promising solution to this problem lies in solar fuels, which has seen a steadily growing interest since the discovery of photocatalysis over 45 years ago.<sup>1</sup> The existing literature offers a wide scope of research ranging from materials development for enhanced electrode performance,<sup>2,3</sup> to comprehensive studies of system designs<sup>4-10</sup> and their limitations.<sup>11-15</sup> Solar fuels can be produced by driving electrolysis of common compounds using the photovoltaic (PV) effect, for example, hydrogen can be produced by electrolyzing water, while a variety of hydrocarbons can be produced from electrolysis of carbon dioxide. There are two generic approaches to assemble a solar electrolysis device. One is to immerse a photo-sensitive electrode in an

electrolyte exposed to sun light, referred to as an integrated photoelectrochemical cell (PEC). On the other hand, it is also possible to power an electrolyzer *via* an independent PV array, making a decoupled photovoltaic electrochemical cell (PV-EC) system.<sup>16</sup> While the PEC makes for a simple and compact device design, it carries several well-known and significant limitations, especially the need for chemical compatibility between the electrolyte and the photoelectrode, and the need for a difficult to achieve high voltage photoactive component. PV-ECs offer several advantages, most important of which is the freedom of independent design of the PV source and the electrochemical load (electrolyzer). PECs have not been demonstrated at a commercial scale and is at a much lower technology maturity than PV-EC, which could be implemented at MW scale today. This benefit of independent component design in PV-ECs enabled realizing a large-area 6.5% solar-to-fuel efficiency (SFE) CO<sub>2</sub> electrolyzer, reported by our group,<sup>17</sup> by using an independently designed flow-cell CO<sub>2</sub>-to-CO electrolyzer<sup>18</sup> and commercial SunPower® Si solar cells. Not only does this device exhibit high efficiency for CO<sub>2</sub> electrolysis, but its electrolyzer area of 25 cm<sup>2</sup> is more than two orders of magnitude larger than other record efficiency CO<sub>2</sub> devices.<sup>19,20</sup>

The use of SFE as a measure of device performance has come to be generally accepted as the figure-of-merit against which devices are reported in the literature. For the solar fuel devices described above, it is the ratio of the energy contained in the product gas to the input solar irradiation, given by:

<sup>a</sup>Institute of Energy Conversion, University of Delaware, Newark, DE-19716, USA.  
E-mail: gowrimsri@gmail.com

<sup>b</sup>Dept. of Electrical and Computer Engineering, University of Delaware, Newark, DE-19716, USA

<sup>c</sup>Dept. of Chemical and Biomolecular Engineering, University of Delaware, Newark, DE-19716, USA

<sup>d</sup>ProtonOnSite, 10 Technology Drive, Wallingford, CT-06492, USA

$$\text{SFE} = J_{\text{OP}} \times \frac{\mu_{\text{TH}}}{P_{\text{IN}}} \times \text{FE} \times \eta_{\text{coll}} \quad (1)$$

where FE is faradaic efficiency of the electrolyzer,  $\mu_{\text{TH}}$  is thermodynamic voltage for the electrolysis reaction, *e.g.* H<sub>2</sub>O to H<sub>2</sub> is 1.23 V and CO<sub>2</sub> to CO is 1.34 V,  $J_{\text{OP}}$  is operating current density, and  $P_{\text{IN}}$  is the input solar insolation and  $\eta_{\text{coll}}$  is the efficiency with which the product gases are collected after separation—a term that highlights the importance of efficient product gas separation after electrolysis, preventing any cross-over. This parameter was set to be 1 in the calculations performed for this work for simplicity. Solar electrolysis devices with SFEs as high as 10% have been reported for CO<sub>2</sub> reduction<sup>19</sup> and greater than 30% for water reduction.<sup>21</sup> While SFEs are typically reported at standard testing conditions (STC) of 1000 W m<sup>-2</sup> insolation and 25 °C, it is well known that the operating conditions of these devices in the real world vary quite significantly and erratically from STC. Only very few reports discuss performance of solar electrolysis devices under conditions different from STC.<sup>22,23</sup> A solar electrolysis device is effectively a source-load combination, and while the load's electrical behavior (the current–voltage curve) remains constant with changing atmospheric conditions, the photovoltaic output is very dependent on insolation and operating temperature. This behooves the designer to ensure maximum power transfer between the energy generator and the electrolysis components at all times.

Optimal power delivery with changing insolation can be achieved through decoupled PV-EC architecture by employing electronic power conditioning between the source and the load,<sup>25,26</sup> such as switch-mode DC-voltage regulators with maximum power point tracking (MPPT).<sup>27</sup> Such a device would continuously adjust the operating voltage on the solar array *I*-*V* curve to keep it at the MPP despite changes in insolation and temperature and convert that power to a voltage and current suitably matched to the electrolyzer. These two functions, MPPT at the input and *V* or *I* regulation at the output, are very similar to charge controllers already widely used for PV battery charging.<sup>28</sup> The key difference is that the output would be optimized for the needs of an electrolyzer not a battery. Another more traditional approach to couple PV-ECs for optimum power delivery would be to use inverter-connected PV-arrays to power commercial electrolyzers designed for AC (grid) (termed ‘DC-AC-DC’ conversion in this work). Since all PV inverters provide MPPT on their DC input side, this approach also ensures maximum power delivery, except for additional losses involving conversion of AC power back to DC inside the electrolyzer. It also enables the PV array to either provide energy directly to the grid or to the EC or both in parallel. This has a strong practical value which is not captured in our analysis. A schematic of a PV-EC system showing a variety of coupling configurations is given in Fig. 1.

Additionally, other practical advantages with indirect PV-EC coupling include: (i) addressing variable collection efficiency of electrolyzer product gases due to electrolyzer transient behavior during a typical day or over an entire year,<sup>24</sup> (ii) controlling CO : H<sub>2</sub> ratio in the case of CO<sub>2</sub> electrolysis systems used with Fischer–Tropsch process, (iii) concurrent operation of

electrolyzer with grid-connected PV systems—which has substantial practical and technoeconomic implications besides operating the high-capex electrolyzer at a higher capacity factor (CF) than the average 4 h per day insolation in typical US locations,<sup>14</sup> and (iv) assuaging the challenges associated with electrolyzer and PV degradation<sup>24</sup> that would otherwise lead to a shift in the operating point of the PV-EC, and therefore its coupling efficiency over time, due to the shifted electrolyzer *I*-*V* curve falling off the ‘knee’ portion (constant current) of the solar array *I*-*V* curve (v) on a larger scale, this arrangement of PV-EC as a grid storage mechanism allows for efficient storage of PV or wind electricity, preventing curtailment for productive utilization.

In this work, different coupling strategies available for PV-ECs will be compared by developing a model to generate annual yield of a PV-EC system. We use the *I*-*V* characteristics of the source and the load as the input, and the atmospheric conditions—insolation and ambient temperature—as variables to generate hourly PV-EC product gas output and SFE. We also allow the model to incorporate power conditioning devices in the simulation to quantitatively assess the benefit they offer to the overall performance of the system. This enables a designer to evaluate the field operation of a PV-EC device, giving insight into its realistic performance rather than idealized STC performance. This model is applied to a previously-reported CO<sub>2</sub> flow-cell PV-EC device of 6.5% SFE.<sup>17</sup> It is then extended to a conceptual solar electrolysis system of 2 MW power, designed using industry-standard proton exchange membrane (PEM) water electrolyzers and commercially-available crystalline silicon solar modules. Using these simulations, we compare different coupling strategies available for both lab-scale devices and large-scale systems.

## Model development

**Annual generation—parameters incorporated.** Given a PV-electrolyzer combination optimized for STC operation, the model uses as input the *I*-*V* behavior of the PV component, along with the polarization and FE curves of the electrochemical device. Meteorological data provided by National Renewable Energy Laboratory's National Solar Radiation Database

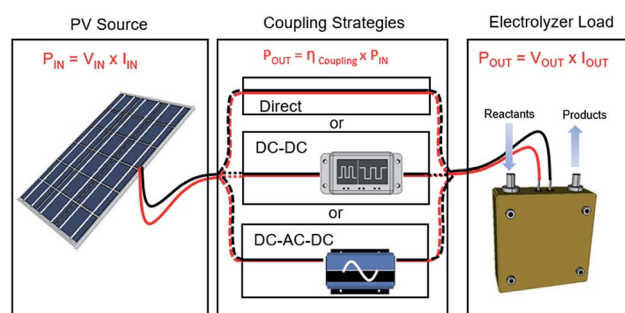


Fig. 1 Schematic of a PV-EC system showing the different coupling strategies possible.  $P_{\text{IN}}$  is the input power generated at the solar array at voltage  $V_{\text{IN}}$ , and current  $I_{\text{IN}}$  and  $P_{\text{OUT}}$  is the power delivered to the electrochemical cell at voltage  $V_{\text{OUT}}$  and current  $I_{\text{OUT}}$ , with a coupling efficiency  $\eta_{\text{coupling}}$ .

(NSRDB)<sup>29</sup> was used to obtain the hourly insolation and temperature data for the specific module deployment method and location. For this work, a module installed at fixed latitude tilt in Wilmington, DE, USA was selected, a mid-latitude location with moderate climate. Using this data, the model computes the solar array  $I$ - $V$  curves as a function of changing solar irradiance and temperature every hour during the entire model year, using the PV  $I$ - $V$  translation equations below.

$$T = T_{\text{module}} = T_{\text{air}} + \frac{\text{NOCT} - 20 \text{ }^\circ\text{C}}{80} \times S \quad (2)$$

$$I_{\text{SC}}(S, T) = \frac{I_{\text{SC,STC}}}{[1 + \alpha(T - 25 \text{ }^\circ\text{C})]} \times \frac{S}{1000 \frac{\text{W}}{\text{m}^2}} \quad (3)$$

$$\Delta V(T) = \beta(T - 25 \text{ }^\circ\text{C}) \quad (4)$$

$$I(V, S, T) = I(V, S_{\text{STC}}) - I_{\text{SC,STC}} + I_{\text{SC}}(S, T) \quad (5)$$

$$V(S, T) = [V_{\text{STC}} - \Delta V] - I(S, T)R_s \quad (6)$$

where  $T_{\text{module}}$  is the module temperature,  $T_{\text{air}}$  is the air temperature, NOCT is the normal operating cell temperature—all given in Celsius,  $S$  is the insolation in  $\text{W m}^{-2}$ ,  $\Delta V$  is the temperature-related drop in array voltage,  $I_{\text{SC}}$  is the short-circuit current while  $I_{\text{SC,STC}}$  is the short circuit current at STC, as given in the module spec sheet,  $\alpha$  is the temperature coefficient for current,  $\beta$  for voltage and  $T$  is the module temperature,  $S_{\text{STC}}$  is 1 sun insolation  $1000 \text{ W m}^{-2}$ ,  $R_s$  is the lumped series resistance of the module isolated from its STC  $I$ - $V$  curve.<sup>30</sup>

The calculated hourly solar array  $I$ - $V$  curves are then overlaid with the electrolyzer polarization curve, giving the operating current  $I_{\text{OP}}(S, T)$ , voltage  $V_{\text{OP}}(S, T)$ , at the intersection of the plots. Using the faradaic behavior of the electrolyzer, the corresponding FE( $S, T$ ) is found, from which the hourly SFE and product gas output are computed as given in eqn (7) and (8). The hourly data is then integrated to compute annual yield and annual average SFE as given in eqn (9) and (10)

$$\text{Hourly SFE, SFE}(S, T) = \frac{\mu_{\text{Th}} \times J_{\text{OP}}(S, T) \times \text{FE}(S, T)}{P_{\text{sun}}} \quad (7)$$

$$\begin{aligned} \text{Hourly gas output (g h}^{-1}\text{), } g(S, T) \\ = \frac{I_{\text{OP}}(S, T) \times 3600 \text{ s h}^{-1} \times \text{FE}(S, T) \times M}{n \times F} \end{aligned} \quad (8)$$

$$\text{Annual average SFE, SFE}_{\text{annual}} = \frac{\sum_{i=1}^N \text{SFE}(S, T)}{N} \quad (9)$$

$$\begin{aligned} \text{Annual gas output (kg y}^{-1}\text{), } G(S, T) &= \int_{t_1}^{t_2} g(S, T) dt \\ &= \sum_{i=1}^N g(S, T) \end{aligned} \quad (10)$$

where  $M$  is the molar mass of the product gas in  $\text{g mol}^{-1}$ ,  $F$  is Faraday's constant in coulomb per mole,  $n$  is the number of

electrons required to make a molecule of the product gas, and  $N$  is the total number of sun hours in the model year which in this study was  $>4000$ .

In addition, the model is designed also to incorporate DC power optimizer devices to the PV-EC system. As described in the introduction, the suggested power optimizer device would consist of DC voltage regulators with MPPT, tailored to the specific PV-EC system. This device actively picks the MPP on the insolation- and temperature-dependent  $I$ - $V$  curve of the PV array and converts the voltage at this power to a voltage on the electrolyzer polarization curve corresponding to the same power. This is graphically represented in Fig. 2 using the power vs. voltage,  $P(V)$ , curves of an example PV-EC system. While the MPPT adjusts the array  $V_{\text{OP}}$  to keep the solar array output at its peak on the power curve, the voltage regulator would translate that  $I$ - $V$  point to fit on the electrolyzer  $P(V)$  curve, *i.e.*, at the same power as the MPP (except for conversion losses related to the regulator), but at a different voltage and current point that falls on the load curve. In the case where the PV and EC devices are directly connected, the operating power point would be where the two  $P(V)$  curves intersect (red dot). The vertical distance  $\Delta P$  between the ordinates at the red and the green points is the difference in the power transferred, showing the improved energy transfer with the use of power optimizer devices over direct-coupled connections during non-standard operating conditions. When integrated over the entire model year, such hourly power differences,  $\Delta P$ , provide the difference in the annual energy delivered to the electrolyzer load between the two coupling configurations. The efficiency of these coupling devices,  $\eta_{\text{coupling}}$ , should also be accounted for strict comparison, although DC-DC switch-mode power converters have efficiencies exceeding 95%.<sup>31</sup> The  $I$ - $V$  transfer function for the power optimizer therefore is:

$$V_{\text{IN}} \times I_{\text{IN}} = \eta_{\text{coupling}} \times V_{\text{OUT}} \times I_{\text{OUT}} \quad (11)$$

where  $V_{\text{IN}} = V_{\text{PV,MPPT}}$  and  $I_{\text{IN}} = I_{\text{PV,MPPT}}$  and  $V_{\text{OUT}}$  and  $I_{\text{OUT}}$  are the output current from the voltage regulator, pre-set to match the EC load curve.

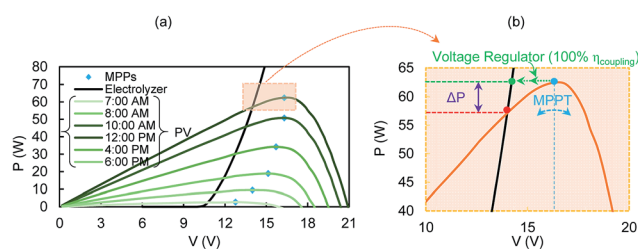


Fig. 2 (a) Power vs. voltage curves of the PV array of an example PV-EC system for changing insolation during a day, overlaid with the power vs. voltage curve of its electrolyzer load. The MPP points are indicated by blue diamonds at peak of each curve. (b) Graphical representation of the performance of a power optimizer device comprising MPPT and a voltage regulator. The red dot represents the operating point (power and voltage) for a directly connected PV-EC, while the green dot represents the operating point in a PV-EC coupled with a DC power optimizer.

The model is developed using the above equations to compute the performance of PV-ECs coupled with power optimizer devices, facilitating their comparison with directly-connected PV-ECs. Using the final (annual) results from this model in addition to a cost analysis, the designer can determine the best coupling strategy for a PV-EC. Cost analysis, however, is not considered in the scope of this paper. The following sections discuss the results calculated from applying the model to the two example PV-EC systems described above.

## 2. Results and discussion

### Annual generation model for lab-scale PV-EC

The model is first applied to a reported 25 cm<sup>2</sup> flow-cell PV-EC for CO<sub>2</sub>–CO solar electrolysis device.<sup>17</sup> The source PV circuit was designed for MPP operation at STC giving an SFE of 7.6%. Empirically determined resistive losses due to non-optimized bench-top connections, reduced measured SFE to 6.5%. H<sub>2</sub>O electrolysis is a competing reaction at the cathode, due to which FE for CO generation is an important metric, which decreases along with SFE with increasing parasitic H<sub>2</sub> production. However, it is important to note that H<sub>2</sub> on its own or together with CO in CO<sub>2</sub> electrolysis is often a desired product for practical purposes (for example for direct use in the Fischer–Tropsch process for hydrocarbon processing), so the SFE given by eqn (1) is a rather conservative estimate that does not credit the energetic value contained in H<sub>2</sub> as a product. While CO and H<sub>2</sub> are the products at the cathode, oxygen effuses at the anode, as given below:

Cathode:

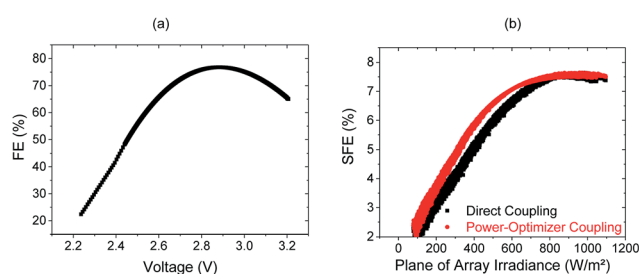
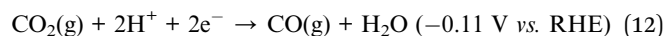
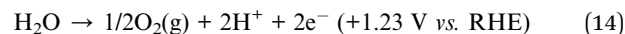
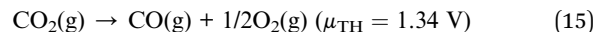


Fig. 3 (a) FE curve of CO<sub>2</sub> electrolyzer used for the model. (b) Calculated SFE plotted against solar irradiation for directly-connected and power-optimizer-coupled PV-ECs.

Anode:



Overall:



where *V* vs. RHE is potential measured against the reversible hydrogen electrode. The *I*–*V* curves of the PV and electrochemical components of this device are input to the developed model.

For this device, we model the direct and power-optimizer configurations, the latter referred to as ‘power optimizer coupling’ as defined above. Since the scale of the device is too small to incorporate the inverter connection in the yield calculations, we omit this coupling strategy for this scenario. Fig. 3(a) shows the FE vs. voltage curve of the electrolyzer used, and Fig. 3(b) shows the resulting SFE calculated by the model as a function of solar insolation for direct- and power-optimizer coupled PV-ECs. This plot generated by the model contains data for every solar hour of each day in the model year, totaling over 4000 data points. While it is evident from eqn (1) that SFE is directly proportional to FE, Fig. 3(b) shows how sensitive SFE is to the FE curve given in Fig. 3(a).

To compare the coupling configurations quantitatively for the CO<sub>2</sub> PV-EC, the numerical results from the simulation, integrated over the entire model year are given in Table 1. The coupling configuration with power optimizer device, has a 5%<sub>relative</sub> higher CO gas output with 9%<sub>relative</sub> increase in SFE (averaged from its performance for the entire year) than that of the direct connection. We note that similar increases in the competing production of H<sub>2</sub> are also predicted with power optimizer coupling. While this PV-EC was designed and reported with SFE of 7.6% at STC (without considering voltage drops consistent with this analysis), the actual SFE averaged for the entire year is 5.1% as shown in Table 1, a decrease of 32%<sub>relative</sub> from the maximum efficiency reported at STC. The effect of the coupling efficiency on the yearly gas output with power optimizer coupling is given in Fig. 4. It is apparent from this figure that if the coupling efficiency—the power conversion efficiency of the DC power optimizer—falls below 96%, it does not offer any advantage to the PV-EC over direct connection.

### Simulating annual generation from a MW-scale PV-EC

In this section, the benefit of power-conditioning devices is applied to large-scale solar fuel generation systems. A

Table 1 Final numerical results from annual model calculations for lab-scale CO<sub>2</sub> PV-EC device with demonstrated 7.6% SFE at STC. H<sub>2</sub> production calculated as competing reaction during CO<sub>2</sub> electrolysis

Coupling type	Avg. SFE (%)	Total CO produced (g y <sup>-1</sup> )	Total H <sub>2</sub> produced (g y <sup>-1</sup> )
Direct coupling	5.06	510	24
DC power-optimizer coupling-100% efficiency	5.52	536	25
DC power-optimizer coupling- $\eta_c = 95\%$	4.59	504	25

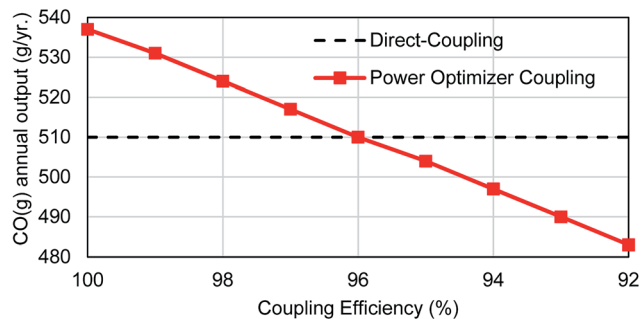


Fig. 4 Annual gas output from the DC power optimizer configuration as a function of its power conversion (coupling) efficiency.

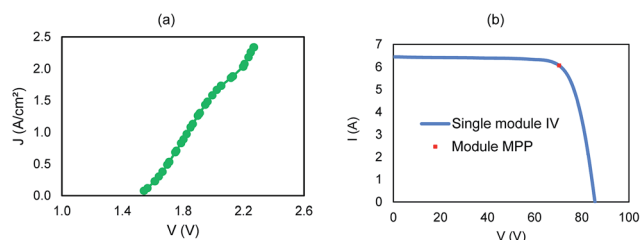


Fig. 5 (a) Single-cell  $J$ - $V$  curve of a PEM water electrolysis cell, (b)  $I$ - $V$  curve of a single SunPower® SPE20-435 module used to power the PEM electrolyzer, with MPP indicated.

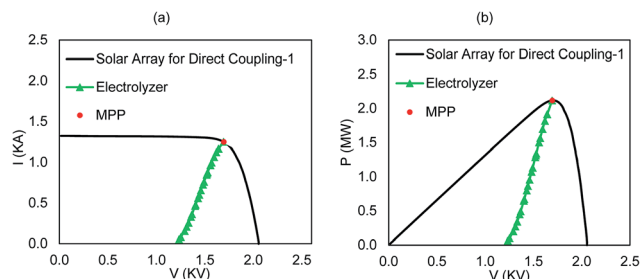


Fig. 6 (a)  $I$ - $V$  curves and (b) power vs. voltage curves of 2.1 MW PEM electrolyzer overlaid with the STC  $I$ - $V$  curve of solar array designed for direct coupling—with MPP indicated.

hypothetical stand-alone solar fuel generation system using a MW-scale PEM water electrolyzer from ProtonOnSite®'s M-series hydrogen generation systems<sup>32</sup> and a PV array consisting of SunPower® solar modules<sup>33</sup> is designed. The  $I$ - $V$  behavior

of a single-cell PEM electrolyzer, given in Fig. 5(a), is scaled up to the power rating of the electrolyzer chosen, 2.1 MW<sub>DC</sub> (Fig. 6(a)). The  $I$ - $V$  curve of a single solar module is given in Fig. 5(b). The electrical specifications of the source and the load used for the model are given in Table 2. We considered a series connection of the electrolyzer stacks for the 2 MW water electrolysis system in this analysis, however, the exact configuration in the actual system can vary.

To design a PV array that is optimally matched to the electrolyzer of interest in the directly-coupled configuration, the 1 sun maximum power voltage and current output of the solar array are matched to the rated peak power of the electrolyzer using their  $I$ - $V$  curves. This is done as follows,

Required number of modules in series per string

$$= \frac{V_{EC,Max}}{V_{MP,1\ sun}} = \frac{1693 V_{DC}}{70.6 V_{DC}} = 23.98 \approx 24 \quad (16)$$

and

$$\begin{aligned} \text{Number of strings in parallel} &= \frac{I_{EC,Max}}{I_{MP,1\ sun}} = \frac{1248 A_{DC}}{6.09 A_{DC}} \\ &= 204.92 \approx 205 \end{aligned} \quad (17)$$

where  $V_{EC,Max}$  and  $I_{EC,Max}$  are the maximum operating voltage and current of the electrolyzer load (comprised of a single 2.1 MW electrolyzer), respectively, and  $V_{MP,1\ sun}$  and  $I_{MP,1\ sun}$  are the maximum power voltage and current of the SunPower® solar module, respectively.<sup>33</sup> The above calculation shows that the PV array would require  $\sim 24$  modules in series per string and  $\sim 205$  strings in parallel, a total of 4920 modules, to provide sufficient voltage and current, respectively, to the load in direct-coupling configuration. It is noted at this point that rounding the exact number of modules in series (or parallel) will slightly offset the position of PV-EC operating point with reference to the PV array MPP on its  $I$ - $V$  curve. This offset can be higher for smaller scale systems, because the 'quanta' of  $\pm 1$  cell or module has more impact. The exact number of solar modules required in series for this arrangement is 23.98 as given by eqn (16). As the incremental difference in the number of solar modules in series due to rounding the exact number from 23.98 to either 23 or 24, is 4% (of 23.98) for this system, the expected offset is relatively small. This decreases further with the number of strings in parallel ( $< 0.5\%$  between 204 and 205 strings). For a smaller scale system, however, this offset can be significant. Consider a ProtonOnsite® 170 KW system powered by the same SunPower® solar panels described above. An optimized direct

Table 2 Electrolyzer and solar module electrical specifications required for PV-EC design

H <sub>2</sub> O electrolyzer specs <sup>32</sup>		Solar module specs <sup>33</sup>	
Maximum operating voltage $V_{EC,Max}$ (V)	1693	$P$ (W)	435
Maximum operating voltage $I_{EC,Max}$ (A)	1248	$V_{MP}$ (V)	70.6
Power rating (MW)	2.11	$I_{MP}$ (A)	6.1
H <sub>2</sub> produced per day (kg H <sub>2</sub> per day)	902	Average power efficiency (%)	20.3
Power consumed per mass of H <sub>2</sub> gas produced (kW h kg <sup>-1</sup> )	59	Module power temperature coefficient (% per °C)	-0.38
		Module area (m <sup>2</sup> )	2.14

connection would require exactly 6.27 panels in series per string and 64.82 strings in parallel. The incremental difference in rounding off the number of modules in series between 6 and 7 is >16%, thereby increasing the operating point offset from the calculated optimum. Thus, for scaled (large) systems, the offset from rounding the number of solar modules in series or parallel is very small compared to small systems. This also means that smaller systems would benefit slightly more with electronic coupling compared to larger systems (as long as these systems are comprised of the same components and are scaled linearly).

For the 2 MW H<sub>2</sub>O electrolysis system, the 24 (series) × 205 (parallel) PV arrangement was selected. Such an arrangement of solar panels, where the number of strings connected in parallel is much larger than the number of modules per string, is converse to traditional PV array configurations where lower currents are driven at high voltages by minimizing the parallel-connected strings. Routing such high currents would require impractically heavy gauge wiring to keep  $I^2R$  losses suitably low. Indirectly-coupled configuration offers the freedom to design the PV array independent of the DC  $I$ - $V$  requirements of the electrolyzer load unlike in direct coupling. This also has the advantage of eliminating the need for bulky wiring across the length of the array, making it a more practical and cost-effective option. While the details are not essential for this modeling, we note that the electrolyzer power requirement would be satisfied in the indirectly connected configuration by arranging the 4920 modules in a conventional PV array configuration.

The results from the model for this case are illustrated as hourly profiles for SFE for a typically sunny and a cloudy day in Fig. 7. The effect of changing insolation on SFE can be seen in Fig. 7(a) and (c), and on hourly module temperature in Fig. 7(b) and (d), for sunny and cloudy days, respectively. It can be seen from these plots that the hourly SFE curve decreases from ~8 am until noon then increases until 5 pm on the sunny day due

to larger temperature dependent module losses (0.38% per °C from Table 2) while the SFE remains moderately constant throughout the cloudy day due to the lower peak module temperature. Comparing these curves against insolation and temperature shows that the ~30% decrease around noon on the sunny day is due to increased module temperature, while drops during dawn and dusk times are due to low insolation. It is also evident from these plots that the power-optimizer coupling has higher SFE at all times.

The system efficiency and H<sub>2</sub> gas output integrated over the entire year for the optimally matched direct coupling ('direct coupling-1') and power optimizer coupling are summarized in Table 3. It is again evident that the PV-EC with power optimizer coupling of 100% coupling efficiency produces 5% higher gas output with a 9%<sub>relative</sub> higher annual average SFE than the optimally matched 'direct coupling-1'. In such a case, the choice between these two coupling strategies should be made by supplementing the generation model results with cost analysis. The results from a DC-AC-DC coupling strategy as described in the introduction applied for this PV-EC are also given in Table 3. For calculating the output with an inverter connection, the dependency of its power conversion efficiency on instantaneous PV output was considered, unlike for DC power optimizer coupling, where a constant electronics power conversion efficiency was used. For the case of DC-AC-DC coupling, the power conversion efficiency as a function of the ratio of instantaneous PV output power to inverter rated power was considered, taken from that of a actual commercial PV inverter.<sup>34</sup> The gas yield and SFE of this configuration are the same as those of direct coupling despite the PV inverter comprising MPPT. It is evident from these results that the losses involving conversion of generated power from DC to AC at the PV array and back from AC to DC in the electrolyzer in the DC-AC-DC configuration compensate any gain provided by the MPPT included in the PV inverter. Fig. 9 shows the effect of coupling efficiency on annual gas production, compared to the other configurations. Similar to the earlier lab-scale device, this configuration loses its advantage at MPPT efficiencies below ~94% efficiency.

The benefit from indirect coupling using power optimizer is small for the PV-ECs when they are optimally matched for direct connection. The value of optimally matching directly-connected

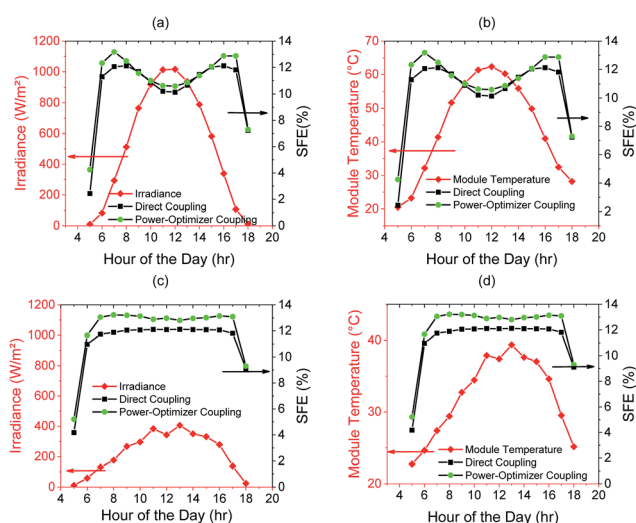


Fig. 7 Hourly efficiency profile shown for a typical sunny day (a) and (b); and a typical cloudy day (c) and (d) in August of the model year, in comparison to hourly irradiation and module temperature, respectively.

Table 3 Tabulated results from the annual generation model applied to 2 MW H<sub>2</sub>O PV-EC for different coupling strategies: optimally matched direct coupling-1, power optimizer coupling with 100% coupling efficiency, DC-AC-DC coupling with 95% DC-AC conversion efficiency, and a slightly mismatched direct coupling-2, with a 25% voltage offset from optimal coupling

Configuration	Avg. SFE (%)	Total H <sub>2</sub> yield (ton H <sub>2</sub> per y)
Direct coupling-1	10.32	70.78
Power optimizer coupling	11.28	74.62
Power optimizer coupling- $\eta_c = 95\%$	10.76	71.36
DC-AC-DC coupling	10.33	70.35
Direct coupling-2	9.16	57.39

Table 4 Solar array layout and electrical specifications for the two directly coupled PV-EC configurations

Configuration	# of solar panels	$P_{MAX}$	$V_{MP}$	$I_{MP}$	Comment
Direct-coupling-1	24 s × 205 p = 4920	2.1 MW	1750 V	1224 A	$V_{MP}$ well matched to EC at STC
Direct-coupling-2	30 s × 164 p = 4920	2.1 MW	2187 V	979 A	$V_{MP}$ mismatched by 25% to EC at STC

PV-ECs and the benefit of using power conditioning devices can be illustrated by taking the same example of the MW-scale PV-EC but now we create an intentional mismatch between a PV array of the same power capacity as above and the electrolyzer. Consider an alternative PV array configuration for direct connection of this PV-EC—slightly mismatched from the optimal setup to have 30 strings with 164 modules per string instead—termed ‘direct connection-2’. Table 4 compares the 2 PV arrays, showing that this suboptimal array design is offset from the previous configuration by 25% on the voltage axis. Its effective  $I$ - $V$  curve and power curve are given in Fig. 8 and the modeled results in Table 3. It can be seen in Fig. 6 that the electrolyzer curve now falls at a lower voltage from the MPP of

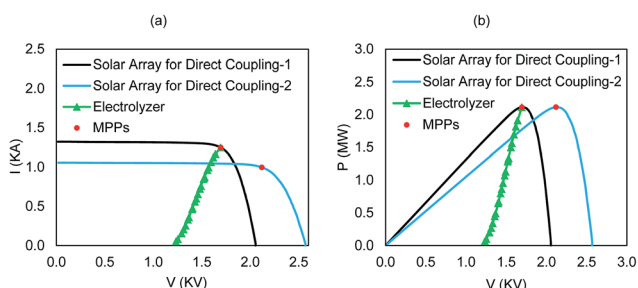


Fig. 8 (a)  $I$ - $V$  curves and (b) power vs. voltage curves of 2.1 MW PEM electrolyzer overlaid with the STC  $I$ - $V$  curves of the two solar arrays designed for direct coupling—one optimally matched (‘direct coupling-1’) and one slightly offset from it (‘direct coupling-2’), with MPPs indicated. The PV array in direct coupling-2 is designed to be 25% mismatched (on the voltage axis) compared to direct coupling-1, as opposed to ~100% STC coupling efficiency of the PV-EC system named ‘direct-coupling-1’.

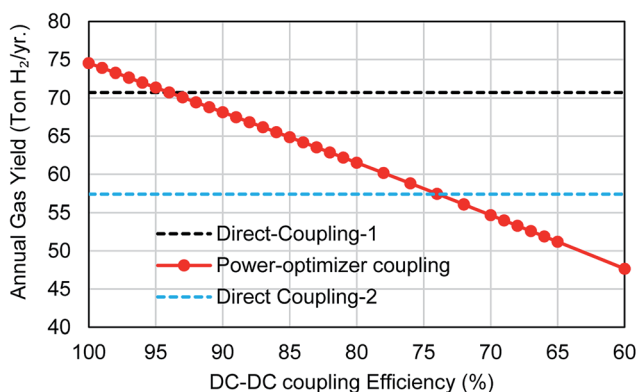


Fig. 9 Annual gas yield of power optimizer coupled PV-EC as a function of the coupling electronics power conversion efficiency. Results from both well matched (direct coupling-1) and mismatched (direct coupling 2) are shown without power coupling. The green line with symbols is for either system using power optimizer.

the solar array. The annual output calculated from this configuration is 20% lower than the optimally configured PV-EC. In that case, employing power optimizer coupling would offer a much higher benefit—a 24% higher gas yield than the mismatched direct coupling, using a coupling device with >94% power conversion efficiency (Fig. 9). From Fig. 9, it is apparent that the coupling efficiency would have to be as low as 75% to match the output from this configuration, much smaller compared to the efficiency of power electronic devices.<sup>31</sup>

### 3. Conclusion

The conventional figure of merit, SFE at STC, is an incomplete metric for solar fuel generation considering the PV device operating conditions are seldom close to STC. In this work, we quantitatively analyzed two system-level aspects of PV-EC's to determine SFE for non-STC conditions: (1) calculating annual fuel output for an outdoor PV-EC using hourly solar irradiance and ambient temperature data for a mid-latitude location with moderate climate (Wilmington DE, USA); and (2) determining the benefits of using power optimizing electronic coupling between the PV array and the electrolyzer to address the realistic situation of a non-optimally matched system. An annual generation model for decoupled solar fuel generation systems was developed and used to compare realistic field performance characteristics. The discrepancy between SFE reported under STC and its yearly average value can be as high as 32%. This disparity arises from the fact that PV-EC is effectively a source-load combination where the load (electrochemical cell) has a constant electrical behavior unlike the source (PV component) that varies with irradiance and temperature. We also quantify the benefits that MPPT with voltage-regulated output can offer, using the annual generation model on a previously-reported lab-scale CO<sub>2</sub> electrolysis device, and a MW-scale H<sub>2</sub>O electrolysis system, conceptually designed for this study. We show that coupling devices improve the annual gas yield by up to 5% even for a PV array that is well matched to the electrolyzer. It was shown using the case of the MW-scale PV-EC that this benefit can be many times higher if the directly connected PV-EC is not optimally power matched. This also highlights the importance of optimal power matching of PV-ECs to maximize their gas yield. The exact quantitative benefit of electronic coupling over direct PV-EC connection is, however, component-specific (based on selection of PV and catalyst technology, their  $I$ - $V$  behavior, geographic location, and scale, among other specifications). To estimate an accurate quantitative benefit of electronic coupling for any given system in general, a similar calculation of system output as given in this study is required for a fair and accurate comparison

among the several possible coupling strategies, including a detailed cost analysis if so warranted.

## Conflicts of interest

The authors declare no competing financial interests.

## Acknowledgements

This work was partially supported under a University of Delaware Energy Institute (UDEI) Innovative Energy Research Grants Program (IERGP). The authors would like to thank Mr Andrew Wright for his help with developing the schematic of Fig. 1.

## References

- 1 A. Fujishima and K. Honda, Electrochemical photolysis of water at a semiconductor electrode, *Nature*, 1972, **238**(5358), 37.
- 2 G. Centi and S. Perathoner, Nanostructured electrodes and devices for converting carbon dioxide back to fuels: advances and perspectives, *Energy Efficiency and Renewable Energy Through Nanotechnology*, Springer, 2011, pp. 561–583.
- 3 Q. Lu, J. Rosen and F. Jiao, Nanostructured metallic electrocatalysts for carbon dioxide reduction, *ChemCatChem*, 2015, **7**(1), 38–47.
- 4 H. Döscher, J. L. Young, J. F. Geisz, J. A. Turner and T. G. Deutsch, Solar-to-hydrogen efficiency: shining light on photoelectrochemical device performance, *Energy Environ. Sci.*, 2016, **9**(1), 74–80.
- 5 C. Ampelli, G. Centi, R. Passalacqua and S. Perathoner, Synthesis of solar fuels by a novel photoelectrocatalytic approach, *Energy Environ. Sci.*, 2010, **3**(3), 292–301.
- 6 M. R. Singh, E. L. Clark and A. T. Bell, Thermodynamic and achievable efficiencies for solar-driven electrochemical reduction of carbon dioxide to transportation fuels, *Proc. Natl. Acad. Sci. U. S. A.*, 2015 Nov 10, **112**(45), E6111–E6118.
- 7 J. Rongé, T. Bosserez, D. Martel, C. Nervi, L. Boarino, F. Taulelle, *et al.*, Monolithic cells for solar fuels, *Chem. Soc. Rev.*, 2014, **43**(23), 7963–7981.
- 8 J. L. Young, M. A. Steiner, H. Döscher, R. M. France, J. A. Turner and T. G. Deutsch, Direct solar-to-hydrogen conversion *via* inverted metamorphic multi-junction semiconductor architectures, *Nat. Energy*, 2017, **2**(4), 17028.
- 9 X. Li, P. Anderson, H. M. Jhong, M. Paster, J. F. Stubbins and P. J. Kenis, Greenhouse gas emissions, energy efficiency, and cost of synthetic fuel production using electrochemical CO<sub>2</sub> conversion and the Fischer–Tropsch process, *Energy Fuels*, 2016, **30**(7), 5980–5989.
- 10 R. E. Blankenship, D. M. Tiede, J. Barber, G. W. Brudvig, G. Fleming, M. Ghirardi, *et al.*, Comparing photosynthetic and photovoltaic efficiencies and recognizing the potential for improvement, *Science*, 2011 May 13, **332**(6031), 805–809.
- 11 D. Bellotti, M. Rivarolo, L. Magistri and A. Massardo, Feasibility study of methanol production plant from hydrogen and captured carbon dioxide, *J. CO<sub>2</sub> Util.*, 2017, **21**, 132–138.
- 12 P. C. Vesborg and B. Seger, Performance limits of photoelectrochemical CO<sub>2</sub> reduction based on known electrocatalysts and the case for two-electron reduction products, *Chem. Mater.*, 2016, **28**(24), 8844–8850.
- 13 Y. Chen, N. S. Lewis and C. Xiang, Operational constraints and strategies for systems to effect the sustainable, solar-driven reduction of atmospheric CO<sub>2</sub>, *Energy Environ. Sci.*, 2015, **8**(12), 3663–3674.
- 14 M. R. Shaner, H. A. Atwater, N. S. Lewis and E. W. McFarland, A comparative technoeconomic analysis of renewable hydrogen production using solar energy, *Energy Environ. Sci.*, 2016, **9**(7), 2354–2371.
- 15 M. T. Patel, M. R. Khan and M. A. Alam, Thermodynamic Limit of Solar to Fuel Conversion for Generalized Photovoltaic–Electrochemical Systems, *IEEE J. Photovolt.*, 2018, **8**(4), 1082–1089.
- 16 T. J. Jacobsson, V. Fjällström, M. Edoff and T. Edvinsson, Sustainable solar hydrogen production: from photoelectrochemical cells to PV-electrolyzers and back again, *Energy Environ. Sci.*, 2014, **7**(7), 2056–2070.
- 17 G. M. Sriramagiri, N. Ahmed, W. Luc, K. D. Dobson, S. S. Hegedus and F. Jiao, Toward a Practical Solar-Driven CO<sub>2</sub> Flow Cell Electrolyzer: Design and Optimization, *ACS Sustainable Chem. Eng.*, 2017, **5**(11), 10959–10966.
- 18 Q. Lu, J. Rosen, Y. Zhou, G. S. Hutchings, Y. C. Kimmel, J. G. Chen, *et al.*, A selective and efficient electrocatalyst for carbon dioxide reduction, *Nat. Commun.*, 2014, **5**, 3242.
- 19 X. Zhou, R. Liu, K. Sun, Y. Chen, E. Verlage, S. A. Francis, *et al.*, Solar-driven reduction of 1 atm of CO<sub>2</sub> to formate at 10% energy-conversion efficiency by use of a TiO<sub>2</sub>-protected III–V tandem photoanode in conjunction with a bipolar membrane and a Pd/C cathode, *ACS Energy Lett.*, 2016, **1**(4), 764–770.
- 20 M. Schreier, L. Curvat, F. Giordano, L. Steier, A. Abate, S. M. Zakeeruddin, *et al.*, Efficient photosynthesis of carbon monoxide from CO<sub>2</sub> using perovskite photovoltaics, *Nat. Commun.*, 2015, **6**, 7326.
- 21 J. Jia, L. C. Seitz, J. D. Benck, Y. Huo, Y. Chen, J. W. D. Ng, *et al.*, Solar water splitting by photovoltaic-electrolysis with a solar-to-hydrogen efficiency over 30%, *Nat. Commun.*, 2016, **7**, 13237.
- 22 J. Bullock, D. F. Srankó, C. M. Towle, Y. Lum, M. Hettick, M. Scott, *et al.*, Efficient solar-driven electrochemical CO<sub>2</sub> reduction to hydrocarbons and oxygenates, *Energy Environ. Sci.*, 2017, **10**(10), 2222–2230.
- 23 S. Haussener, S. Hu, C. Xiang, A. Z. Weber and N. S. Lewis, Simulations of the irradiation and temperature dependence of the efficiency of tandem photoelectrochemical water-splitting systems, *Energy Environ. Sci.*, 2013, **6**(12), 3605–3618.
- 24 R. R. Gutierrez and S. Haussener, Modeling of Concurrent CO<sub>2</sub> and Water Splitting by Practical Photoelectrochemical Devices, *J. Electrochem. Soc.*, 2016, **163**(10), H1008–H1018.
- 25 M. T. Winkler, C. R. Cox, D. G. Nocera and T. Buonassisi, Modeling integrated photovoltaic–electrochemical devices using steady-state equivalent circuits, *Proc. Natl. Acad. Sci. U. S. A.*, 2013, 201301532.

- 26 A. Mohammadi and M. Mehrpooya, A comprehensive review on coupling different types of electrolyzer to renewable energy sources, *Energy*, 2018, **158**, 632–655.
- 27 T. Eswam and P. L. Chapman, Comparison of photovoltaic array maximum power point tracking techniques, *IEEE Trans. Energy Convers.*, 2007, **22**(2), 439–449.
- 28 H. Masheleni and X. Carelse, Microcontroller-based charge controller for stand-alone photovoltaic systems, *Sol. Energy*, 1997, **61**(4), 225–230.
- 29 NREL's National Solar Radiation Database (NSRDB), <https://nsrdb.nrel.gov/nsrdb-viewer>, accessed July 17th, 2018.
- 30 S. S. Hegedus and W. N. Shafarman, Thin-film solar cells: device measurements and analysis, *Prog. Photovoltaics*, 2004, **12**(2–3), 155–176.
- 31 B. K. Bose, Power electronics and motor drives recent progress and perspective, *IEEE Trans. Ind. Electron.*, 2009, **56**(2), 581–588.
- 32 Proton OnSite®'s M Series Hydrogen Generation Systems Specification Sheet, [http://www.protononsite.com/sites/default/files/2018-04/PD-0600-0119\\_rev\\_a.pdf](http://www.protononsite.com/sites/default/files/2018-04/PD-0600-0119_rev_a.pdf), accessed July 17th, 2018.
- 33 SunPower®'s E-series module data sheet, <https://us.sunpower.com/sites/sunpower/files/media-library/data-sheets/ds-e20-series-435-commercial-solar-panels.pdf>, accessed July 17th, 2018.
- 34 <http://www.hitachi-hirel.com/products/solar-inverters/hiverternp201i-series>.